INORGANIC CHEMISTRY
FRONTIERS

RESEARCH ARTICLE

View Article Online
View Journal | View Issue

Cite this: *Inorg. Chem. Front.*, 2023, **10**, 4544

Photocatalytic water oxidation over $LaWO_{0.6}N_{2.4}$ mesoporous single crystals under visible and near-infrared light illumination†

Lin Yang, Hui Duan* and Xiaoxiang Xu *

Received 18th May 2023,
Accepted 26th June 2023

DOI: 10.1039/d3qi00924f

rsc.li/frontiers-inorganic

Narrow-bandgap perovskite oxynitrides emerge as a promising class of inorganic photocatalysts to store solar energy in chemical fuels. However, conventional synthetic routes generally introduce a high defect concentration in these compounds, particularly at grain boundaries (GBs), which also intercept charge transportation, thus severely undermining the photocatalytic performance. Herein, we demonstrate that GB-free porous single crystals (PSCs) of narrow bandgap semiconductor $LaWO_{0.6}N_{2.4}$ can be prepared by the topotactic conversion of $BiLaWO_6$. Due to a high structural homogeneity and porosity, $LaWO_{0.6}N_{2.4}$ PSCs deliver a good photocatalytic activity for oxidizing water into O_2 even under near-infrared light illuminations. Under optimal conditions, an apparent quantum efficiency (AQE) value as high as 0.13% at 800 ± 20 nm were achieved, being the first near-infrared-light active oxynitride for photocatalytic water oxidation thus far. Steady overall water splitting into stoichiometric H_2 and O_2 has also been realized in a Z-scheme system employing $LaWO_{0.6}N_{2.4}$ PSCs as the O_2-evolution moiety under visible light insolation. These results not only justify that PSCs serve as an ideal platform to trigger the photocatalytic performance of oxynitrides with high defects content but also attract great attention upon W-based perovskite oxynitrides for solar energy conversions.

Introduction

Water cleavage over particulate photocatalysts offers a promising means to store intermittent solar energy into hydrogen energy, which is the ideal fuel for the future.[1–5] To this end, narrow bandgap semiconductors that can harvest a significant portion of the solar spectrum, *i.e.*, visible to near infrared, are strongly desired.[6–12] However, narrow bandgap semiconductors can generally produce low energetic photocarriers; thereby, it is very challenging to drive the uphill-type water splitting reactions.[13,14] For instance, a semiconductor with light absorption threshold of 800 nm can only produce photocarriers with an energy gap of 1.55 eV, being very close to the minimal demand of 1.23 eV for overall water splitting reactions. Thus, it becomes imperative to minimize energy loss during photocarrier transportation and transfer steps over narrow bandgap semiconductors for photocatalytic water splitting reactions.

Among various narrow bandgap semiconductors reported, d^0-type transition metal perovskite oxynitrides, *i.e.*, $AM(O,N)_3$ (A = Ca, Sr, Ba, and La; M = Ti, Nb, Ta, and W), have gained considerable attention as photocatalysts for water splitting owing to their intensive visible light absorption, chemical robustness, and photocatalytic activity for water redox reactions.[15–18] In particular, $LaWO_{0.6}N_{2.4}$ shows strong light absorption from visible to near infrared region as an ideal photocatalyst to convert solar energy.[19,20] This is partly attributed to its high N/O ratio that substantially uplifts the valence band top, thereby reducing the threshold for light harvest. Notwithstanding such appealing properties, $LaWO_{0.6}N_{2.4}$ is subject to poor photocatalytic activities.[21] This can be understood by the high electronegativity of W^{6+} that is susceptible to induce a high concentration of defects (W^{5+}, W^{4+} *etc.*) during high-temperature ammonolysis. These defects have been widely recognized as charge trapping and recombination centers that greatly undermine the photocatalytic activity.[18,22,23] Things become even worse as powdery $LaWO_{0.6}N_{2.4}$ often contains copious grain boundaries (GBs).

Shanghai Key Lab of Chemical Assessment and Sustainability, School of Chemical Science and Engineering, Tongji University, Shanghai, 200092, China.
E-mail: dhui@tongji.edu.cn, xxxu@tongji.edu.cn; Tel: +86-21-65982670, +86-21-65986919

† Electronic supplementary information (ESI) available: XRD patterns, SEM-EDS analyses; Raman spectra; Tauc plot analysis; XPS spectra; photocatalytic data; refined unit cell parameters and bandgap values; elemental compositions; BET analysis. See DOI: **https://doi.org/10.1039/d3qi00924f**

These GBs not only are enriched with defects but also serve as interceptions to the photocarrier transportation across neighboring particles.[24–29] Accordingly, it implicates a useful strategy to upgrade the photocatalytic performance of $LaWO_{0.6}N_{2.4}$ by eliminating the GBs as well as defects.

In general, $LaWO_{0.6}N_{2.4}$ is prepared by high-temperature ammonolysis using shapeless precursor powders of $La_2W_2O_9$, $La_4W_3O_{15}$ and amorphous metal oxides.[19–21] The irregular precursor particles with random exposure of crystal facets are characterized with uncontrolled grain growth during high-temperature ammonolysis, resulting in abundant GBs in the product. Seeking alternative precursors with specific exposure of crystal facets would be a useful means to regulate grain growth as well as to avoid GBs. We have previously used Sillén–Aurivillius type oxyhalides as the precursors to prepare porous single crystals (PSCs) of perovskite oxynitrides that are free of GBs.[30–33] In this work, we adopt a layered compound $BiLaWO_6$ as the precursor to synthesize $LaWO_{0.6}N_{2.4}$ PSCs for the first time. $BiLaWO_6$ contains perovskite blocks and can be topotactically transformed into $LaWO_{0.6}N_{2.4}$ during high-temperature ammonolysis. The as-prepared $LaWO_{0.6}N_{2.4}$ PSCs do not contain GBs and are active to drive water oxidation reactions under visible and even near infrared light illumination. Its potential as a water splitting photocatalyst is also exemplified by a Z-scheme overall water splitting system that employs $LaWO_{0.6}N_{2.4}$ PSCs as the O_2-evolution moiety.

Experimental

Materials synthesis

Preparation of $BiLaWO_6$ precursor. The $BiLaWO_6$ precursor was synthesized based on a molten-salt assisted flux method. Briefly, 0.6518 g La_2O_3 (Aladdin, 99.99%), 0.9329 g Bi_2O_3 (Aladdin, 99.9%), and 0.9292 g WO_3 (Aladdin, 99.8%) were blended thoroughly with 1.4985 g KCl (SCR, 99.5%) using an agate mortar and a pestle. The mixtures were then transferred into an alumina crucible and were annealed at 1073 K for 1 h in a muffle furnace. After cooling naturally to room temperature, the product powders were rinsed with deionized water and ethanol repeatedly to remove residual KCl. Pale yellow powders were collected and dried at 353 K overnight for further use.

Preparation of $LaWO_{0.6}N_{2.4}$ porous single crystals (PSCs). $LaWO_{0.6}N_{2.4}$ PSCs were prepared by topotactically transforming $BiLaWO_6$ *via* high-temperature ammonolysis. Specifically, 0.2 g freshly prepared $BiLaWO_6$ powders were mounted into a tube furnace using an alumina boat. The furnace was then heated up to 1173 K (heating rate ~ 7 K min^{-1}) under flowing ultrapure ammonia (flow rate ~ 200 mL min^{-1}, Jiaya Chemicals, 99.999%) and was kept at 1173 K for 10 h. The furnace was then cooled naturally to room temperature under flowing ammonia. The resultant black powders were collected and labelled as $LaWO_{0.6}N_{2.4}$-P. For comparison, $LaWO_{0.6}N_{2.4}$ was also prepared under the same conditions using conventional $La_2W_2O_9$ as the precursor. The $La_2W_2O_9$ powders were synthesized by calcining the mixtures of 1.3035 g La_2O_3 (Aladdin, 99.99%) and 1.8584 g WO_3 (Aladdin, 99.8%) at 1373 K for 24 h according to a previous report.[19] The resultant product after ammonolysis was labelled as $LaWO_{0.6}N_{2.4}$-S for discrimination.

Preparation of Rh-doped $SrTiO_3$ ($SrTiO_3$:Rh). Rh-doped $SrTiO_3$ ($SrTiO_3$:Rh) was used as an H_2-evolution moiety for Z-scheme water splitting reactions. $SrTiO_3$:Rh powders were prepared according to a previous report.[34] To promote H_2-evolution reactions, Ru (0.5 wt%) was photodeposited onto $SrTiO_3$:Rh as a cocatalyst. Briefly, 0.2 g $SrTiO_3$:Rh powders and 1 mL $RuCl_3$ aqueous solution (1 mg_{Ru} mL^{-1}) were dispersed into 20 mL methanol aqueous solution (50 vol%) to form suspensions under sonication. After constant irradiation for 7 h using a xenon lamp (300 W, PLX-SXE300, Perfect Light), the suspensions were centrifuged and the precipitates were washed with deionized water and ethanol several times before drying in air at 353 K overnight.

Materials characterization

The freshly prepared sample powders were subject to a series of analysis to understand their physical and chemical properties. X-ray powder diffraction (XRD) analysis was conducted on a Bruker D8 Focus diffractometer (Bruker, Germany) to check the phase purity and crystal structure using Cu Kα_1 (λ = 1.5406 Å) and Cu Kα_2 (λ = 1.5444 Å) as the incident radiation. The general step size and duration time for data collection were set as 0.01 and 0.1 s at each step, respectively. The XRD data collected were used for Rietveld refinement based on General Structure Analysis System (GSAS) software package to investigate the crystal structure.[35] A pseudo-Voigt function was adopted for profile fitting and the first type Chebyshev polynomial was applied for background fitting. The oxygen and nitrogen content in sample powders were determined through an Elemental Analyzer (Unicube, Elementar, Germany). The cations in the samples were quantified by inductively coupled plasma optical emission spectrometry (ICP-OES, Agilent 720ES). Sample powders were further inspected under a field emission scanning electron microscope (Hitachi S4800, Japan) equipped with an energy-dispersive X-ray spectroscopy (EDS) analysis system and a transmission electron microscope (TEM, JEOL JEM-2100, Japan). The Raman spectra of the as-obtained sample powders were collected on a UV Raman spectrometer (Renishaw inVia). The specific surface area of the sample powders was calculated according to the data collected on a NOVA 2200e adsorption instrument (Quantachrome, USA) using the Brunauer–Emmett–Teller (BET) model. Ultraviolet-visible-near infrared diffuse reflectance spectra (UV-Vis-NIR DRS) were collected on a UV-Vis-NIR spectrophotometer (Agilent Cary 5000) equipped with an integrating sphere. The non-absorbing reference material was $BaSO_4$. An X-ray photoelectron spectrometer (XPS, AXIS Ultra DLD, Japan) with a monochromatic Al Kα X-ray source was used to examine the surface state of the sample powders. The adventitious carbon C 1s peak at 284.7 eV was adopted for signal adjustment.[36] XPS PEAKFIT software was used for XPS data fitting. The fitting was performed by referring to Gaussian–Lorentzian (Lorentzian weighting of 20%) type peak shape and a Shirley-type background. Mott–Schottky (MS) experiments were conducted on a Zahner electrochemical workstation based on a three-electrode configuration setup. The working electrodes were fabricated through the electrophoretic deposition method using fluorine-doped tin oxide (FTO) glasses as the conductive substrate.[37] The prepared photoelectrode, Pt foil (10 × 10 mm), and Ag/AgCl electrode (saturated KCl) were used as the working, counter, and reference electrodes, respectively. Aqueous KOH solution (0.1 M, pH = 13) was applied as the electrolyte. Flat band potentials were obtained by extracting the capacitance data from the electrochemical impedance spectra (EIS) at 500, 1000, and 2000 Hz within a potential window of −0.3 to 0.8 V *vs.* RHE.

Photocatalytic water splitting

Photocatalytic water-splitting experiments were conducted in a top-irradiation-type reactor connected to a gas-closed circulation and evacuation system (Labsolar-6A, Perfect Light). In brief, proper amounts of CoO_x were thermally loaded onto sample powders as a cocatalyst by referring to a previous report.[15] Subsequently, 0.1 g sample powders loaded with CoO_x cocatalyst and 0.2 g La_2O_3 (pH buffer, Aladdin, 99.9%) were dispersed into 100 mL silver nitrate aqueous solution (0.05 M) under constant magnetic stirring. The so-formed suspensions were transferred into the reactor. The reactor temperature was maintained at 281 K using a water jacket. After evacuation for 45 min to remove the dissolved air, the reactor was illuminated from the top by a 300 W xenon lamp (PLX-SXE300, Perfect Light) coupled with either a UV ($\lambda \geq 420$ nm) or visible light ($\lambda \geq 800$ nm) cutoff filter. For the determination of apparent quantum efficiency (AQE), bandpass filters at 420 nm, 450 nm, 500 nm, 550 nm, 600 nm, 700 nm, and 800 nm (Perfect Light) were respectively used to obtain monochromatic light. The photon flux was quantitatively determined by a quantum meter (Apogee MP-300, USA). The gas component within the reactor was analyzed by an on-line gas chromatograph (GC2014C, SHIMADZU, Japan) installed with a 5 Å molecular sieve column, TCD detector, and Ar as the carrier gas. The AQE for oxygen production was calculated based on the following equation (eqn (1)).

$$\mathrm{AQE} = \frac{4 \times \text{mol of oxygen production per hour}}{\text{mol of photon flux per hour}} \times 100\% \qquad (1)$$

For Z-scheme water splitting, 50 mg Ru-loaded $SrTiO_3$:Rh and 50 mg CoO_x-loaded $LaWO_{0.6}N_{2.4}$ were ultrasonically dispersed into 100 mL $FeCl_3$ aqueous solution (2 mM). Several drops of HCl aqueous solution (0.1 M) were added to adjust the pH value to about 2.5. Pre-illumination lasted for about 1 h was conducted before overall water splitting experiment, which induces the formation of Fe^{2+}/Fe^{3+} redox couple by the partial conversion of Fe^{3+} to Fe^{2+}. The Z-scheme water splitting experiments were performed similar to previous experiments using a 300 W xenon lamp (PLX-SXE300, Perfect Light) coupled with a UV cutoff filter ($\lambda \geq 420$ nm).

Results and discussion

Crystal structures and morphologies

The precursor $BiLaWO_6$ is an isostructural compound to Bi_2WO_6, an archetypal Aurivillius compound with the general formula $[Bi_2O_2][A_{n-1}B_nO_{3n+1}]$ ($n = 1$). The structure of $BiLaWO_6$ comprises alternative stacking of $[Bi(La)_2O_2]^{2+}$ fluorite layer and $[WO_4]^{2-}$ perovskite layer.[38,39] WO_6 polyhedrons in the $BiLaWO_6$ are connected in a corner-type manner, which is topotactically similar to those of $LaWO_{0.6}N_{2.4}$ (Fig. 1b). X-ray powder diffraction (XRD) analysis and corresponding Rietveld refinement confirm the successful preparation of $LaWO_{0.6}N_{2.4}$ using $BiLaWO_6$ as the precursor (Fig. 1a, b, Fig. S1 and Table S1†). The possible transformation mechanism is proposed as follows: $BiLaWO_6$ undergoes gradual Bi loss during the high-temperature ammonolysis since Bi^{3+} cations are susceptible to reduction into elemental Bi, which subsequently evaporates at high temperatures. The residual perovskite blocks then stack facilely without substantial atom migrations/rearrangements to form $LaWO_{0.6}N_{2.4}$ (Fig. 1c). As no long-range migration of La and W atoms are involved during transformation, the product $LaWO_{0.6}N_{2.4}$ particles can retain the morphologies of the precursor. This is evidently supported by the field-emission scanning electron microscopic (FE-SEM) characterization (Fig. 1d, e, and Fig. S2†). As can be seen from the FE-SEM images, the ribbon-like morphologies of $BiLaWO_6$

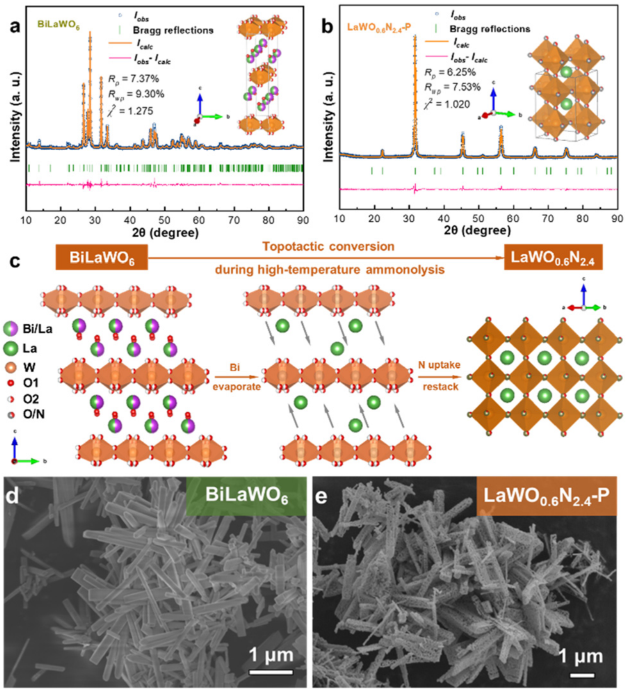

Fig. 1 Observed and calculated X-ray powder diffraction (XRD) patterns of (a) $BiLaWO_6$ and (b) $LaWO_{0.6}N_{2.4}$-P, refined reasonable agreement factors (R_p, R_{wp}, and χ^2) are inseted; images of their refined crystal structures are also included; (c) the proposed structural evolution mechanism from $BiLaWO_6$ to $LaWO_{0.6}N_{2.4}$; field-emission scanning electron microscopy (FE-SEM) images for (d) $BiLaWO_6$ and (e) $LaWO_{0.6}N_{2.4}$-P.

are well-maintained in the product $LaWO_{0.6}N_{2.4}$, thus verifying our proposed mechanisms. The high porosity of $LaWO_{0.6}N_{2.4}$ particles can be attributed to the evaporation of Bi as well as O/N replacements during high-temperature ammonolysis. The product $LaWO_{0.6}N_{2.4}$ is then denoted as $LaWO_{0.6}N_{2.4}$-P to be discriminated from the one produced from $La_2W_2O_9$ (denoted as $LaWO_{0.6}N_{2.4}$-S).

Although $LaWO_{0.6}N_{2.4}$ can be produced from different precursors (Fig. 3a, Fig. S3 and Table S2†), their microstructures are distinct and are strongly correlated with the precursors used. The $LaWO_{0.6}N_{2.4}$-S powders contain irregularly-shaped grains with a size of ~50 nm and are randomly compacted to form bulky particles as large as several microns (Fig. 2a). Although $LaWO_{0.6}N_{2.4}$-S powders are porous, GBs between neighbouring grains can be easily identified (Fig. 2b). This is in sharp contrast to $LaWO_{0.6}N_{2.4}$-P, which contains no GBs (Fig. 2c–e). This is also confirmed by TEM analysis. As can be seen from Fig. 2e, a single $LaWO_{0.6}N_{2.4}$-P particle contains three-dimensionally interconnected pores and is lacking of GBs in its skeletons. The single $LaWO_{0.6}N_{2.4}$-P particle is of high crystallinity whose crystal structure is coherent throughout the entire particle, as revealed by the high-resolution TEM image (HRTEM) (Fig. 2f) and selected area electron diffraction (SAED) pattern (Fig. 2g). The high porosity of both $LaWO_{0.6}N_{2.4}$-P and $LaWO_{0.6}N_{2.4}$-S is further confirmed by BET analysis, which shows hysteresis between the desorption and adsorption profiles (Fig. 3b). The pore size distribution analysis (Fig. 3b inset and Table S3†) indicates that most pores fall into the region of mesopores (<50 nm). These results jointly suggest that $LaWO_{0.6}N_{2.4}$ PSCs can be successfully prepared from $BiLaWO_6$ *via* the topotactic transformation mechanisms.

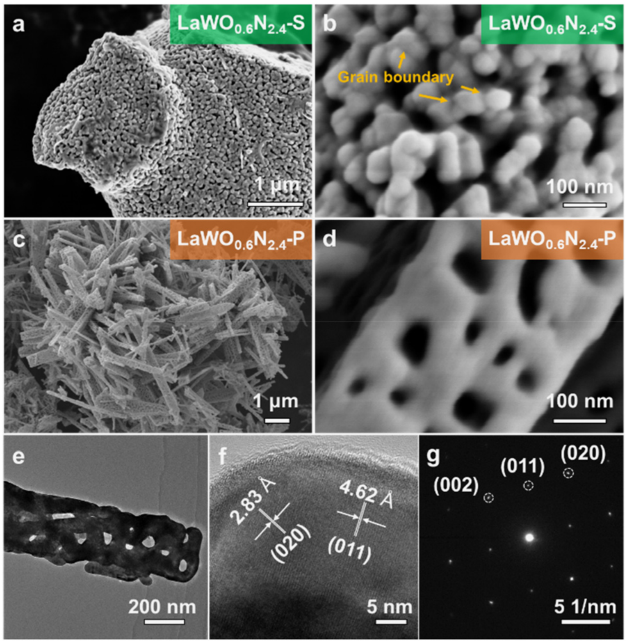

Fig. 2 FE-SEM images of (a and b) $LaWO_{0.6}N_{2.4}$-S and (c and d) $LaWO_{0.6}N_{2.4}$-P under different magnifications; GBs are marked by yellow arrows; (e) TEM image of a single $LaWO_{0.6}N_{2.4}$-P; (f) HRTEM image of $LaWO_{0.6}N_{2.4}$-P, lattice fringes marked correspond to (020) and (011) facets of $LaWO_{0.6}N_{2.4}$-P; (g) SAED pattern of a single $LaWO_{0.6}N_{2.4}$-P.

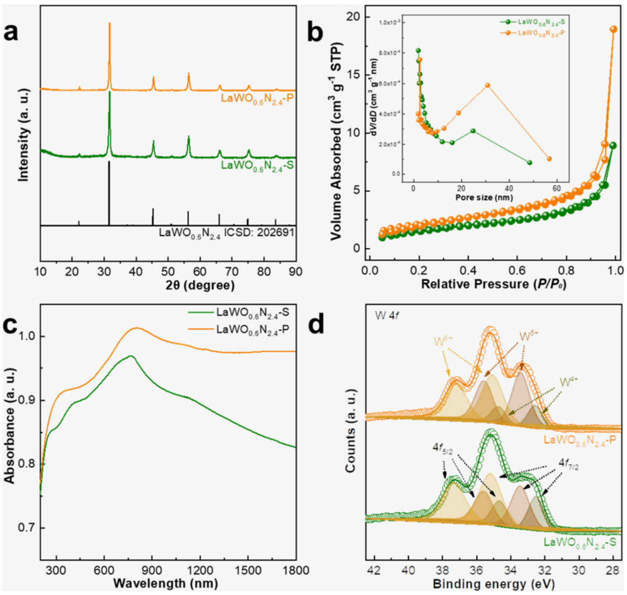

Fig. 3 (a) XRD patterns for $LaWO_{0.6}N_{2.4}$-S and $LaWO_{0.6}N_{2.4}$-P, standard pattern of $LaWO_{0.6}N_{2.4}$ (ICSD: 202691) is also included for comparison; (b) BET analyses of $LaWO_{0.6}N_{2.4}$-S and $LaWO_{0.6}N_{2.4}$-P; the inset displays their pore size distributions; (c) ultraviolet-visible-near infrared diffuse reflectance spectra (UV-Vis-NIR DRS) for $LaWO_{0.6}N_{2.4}$-S and $LaWO_{0.6}N_{2.4}$-P; (d) X-ray photoelectron spectroscopy (XPS) W 4f spectra of $LaWO_{0.6}N_{2.4}$-S and $LaWO_{0.6}N_{2.4}$-P.

Surface state and UV-Vis-NIR spectra

Given the distinct morphologies between $LaWO_{0.6}N_{2.4}$-S and $LaWO_{0.6}N_{2.4}$-P, we continue our exploration on their optical and surface properties. The UV-Vis-NIR DRS spectra of $LaWO_{0.6}N_{2.4}$-S and $LaWO_{0.6}N_{2.4}$-P powders are illustrated in Fig. 3c. Both compounds exhibit intense absorption in the measured range from 250 nm to 1800 nm, which is consistent with the black color of the sample powders. In particular, $LaWO_{0.6}N_{2.4}$-P appears to have stronger light absorption than $LaWO_{0.6}N_{2.4}$-S although their structure and composition are essentially identical. The slightly higher light absorption of $LaWO_{0.6}N_{2.4}$-P might be rationalized by its higher porosity than $LaWO_{0.6}N_{2.4}$-S, which favors more light reflection in the inner part of the particle. The bandgap is then deduced by a modified Tauc plot analysis method, which suggests a light absorption threshold of ~1.2 eV of both compounds (Fig. S4†), consistent with the value reported.[19,21] The intense absorption above 1050 nm is therefore assignable to various types of defect absorption, which is frequently noticed for oxynitrides. The existence of high concentration of defects is also indicated by XPS analysis shown in Fig. 3d, Fig. S5, and Table S4.† Specifically, the W 4f state contains three distinct spin–orbit pairs assignable to the W^{6+}, W^{5+}, and W^{4+} species.[19] Nevertheless, there is slight variation in the content of these species between $LaWO_{0.6}N_{2.4}$-S and $LaWO_{0.6}N_{2.4}$-P. For instance, $LaWO_{0.6}N_{2.4}$-P has a high W^{5+} content (41.5%) while $LaWO_{0.6}N_{2.4}$-S is enriched with W^{4+} (20.7%). These differences might be related to the different precursors used for synthesis. $BiLaWO_6$ might serve partially as a sacrificial agent due to the reduction of Bi^{3+}, which helps to reduce the risks of W^{6+} reduction.

Photocatalytic performance and band edge positions

The photocatalytic performance of $LaWO_{0.6}N_{2.4}$-P and $LaWO_{0.6}N_{2.4}$-S was then evaluated by comparing their O_2-evolution activity using visible ($\lambda \geq 420$ nm) and infrared light ($\lambda \geq 800$ nm) illumination. 1 wt% CoO_x was thermally deposited as a cocatalyst and $AgNO_3$ was used as the electron scavenger. Control experiments without any key component of either photocatalyst, light sources, or water did not produce any detectable oxygen gases, thereby excluding any O_2-evolving spontaneous reactions. Instantaneous oxygen signals were detected when sample powders were illuminated in the presence of $AgNO_3$ aqueous solution, confirming that real photocatalytic processes (Fig. 4 and Fig. S6†). A concomitant N_2-evolution was also observed for both samples, which was attributed to photooxidative self-decomposition similar to other oxynitrides.[19,40,41] Impressively, $LaWO_{0.6}N_{2.4}$-P photocatalyzed more than 3-fold O_2-evolution when compared with $LaWO_{0.6}N_{2.4}$-S (Fig. 4a). As both compounds are of high structural and compositional similarity, such improved activity and stability is probably related to the peculiar microstructures of PSCs. More importantly, $LaWO_{0.6}N_{2.4}$-P is capable of photocatalytic water oxidation into O_2 under infrared light illumination ($\lambda \geq 800$ nm), underscoring the capability to substantially extend the useable bandwidth of solar spectrum (Fig. 4b).

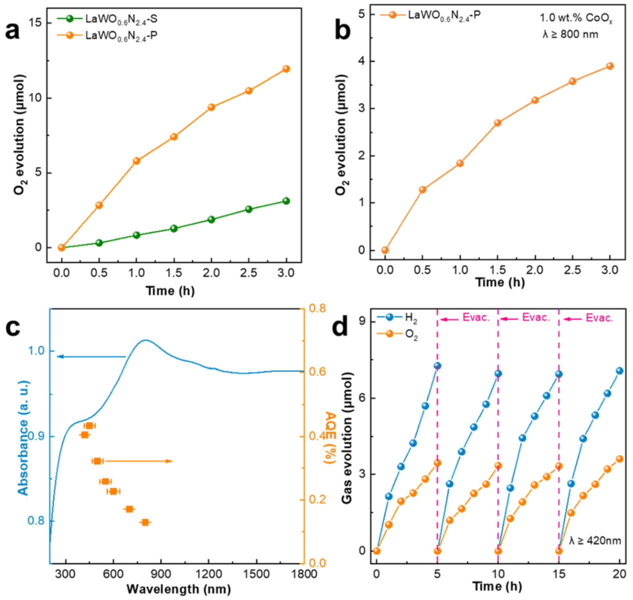

Fig. 4 (a) Temporal O_2 and N_2 evolution over $LaWO_{0.6}N_{2.4}$-S and $LaWO_{0.6}N_{2.4}$-P with 1 wt% CoO_x as a cocatalyst under visible light illumination ($\lambda \geq 420$ nm) in 0.05 M $AgNO_3$ aqueous solution, 0.2 g La_2O_3 was added as the pH buffer; (b) temporal O_2 and N_2 production over $LaWO_{0.6}N_{2.4}$-P loaded with 1 wt% CoO_x as a cocatalyst under infrared light illumination ($\lambda \geq 800$ nm) in 0.05 M $AgNO_3$ aqueous solution containing 0.2 g La_2O_3; (c) action spectra of $LaWO_{0.6}N_{2.4}$-P loaded with 1 wt% CoO_x for O_2 production; (d) Z-scheme overall water splitting under visible light illumination ($\lambda \geq 420$ nm) based on $LaWO_{0.6}N_{2.4}$-P (loaded with 1 wt% CoO_x) as the O_2-evolution moiety and $SrTiO_3$:Rh (loaded with 0.5 wt% Ru) as the H_2-evolution moiety, Fe^{2+}/Fe^{3+} redox couple (0.002 M) was used as the redox shuttle, and evacuation was performed every 5 h.

The photocatalytic activity of $LaWO_{0.6}N_{2.4}$-P was further optimized by varying the amounts of CoO_x cocatalyst deposited (Fig. S6†). 1 wt% CoO_x loading delivered the highest activity and was adopted for the determination of apparent quantum efficiency (AQE). The action spectra of $LaWO_{0.6}N_{2.4}$-P, *i.e.*, AQE *vs.* wavelength, are illustrated in Fig. 4c, and the data for calculating AQE were tabulated in Table S5.† The $LaWO_{0.6}N_{2.4}$-P approaches an AQE as high as 0.13% at 800 ± 20 nm, which is the first near-infrared-light active oxynitride for photocatalytic water oxidation thus far. The large deviation of the AQE profile with UV-Vis-NIR spectra can be explained by the defect's high absorption that superimposed the intrinsic light absorption of $LaWO_{0.6}N_{2.4}$. The repeated photocatalytic test was performed in 0.05 M sodium persulfate aqueous solution, which suggests a durable production of O_2 from $LaWO_{0.6}N_{2.4}$-P (Fig. S7†). The attempts to photocatalyze water reduction into H_2 failed using both $LaWO_{0.6}N_{2.4}$-P and $LaWO_{0.6}N_{2.4}$-S. This can be explained by the inappropriate conduction band edge alignment of $LaWO_{0.6}N_{2.4}$, which is more positive than the water reduction potential, as revealed by the band edge analysis (Fig. 5). Mott–

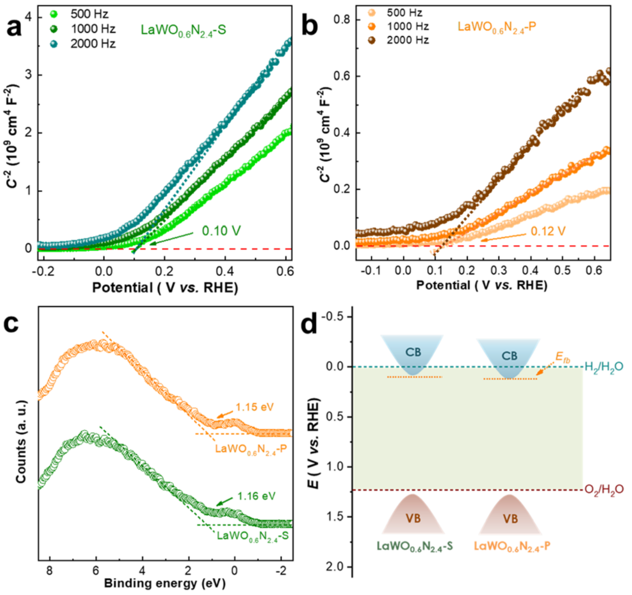

Fig. 5 Mott–Schottky (MS) plot for (a) $LaWO_{0.6}N_{2.4}$-S and (b) $LaWO_{0.6}N_{2.4}$-P photoelectrodes, flat band potential is determined by extrapolating the MS curve down to energy axis; (c) XPS valence band scan for $LaWO_{0.6}N_{2.4}$-S and $LaWO_{0.6}N_{2.4}$-P; (d) schematic representation of band edge positions for $LaWO_{0.6}N_{2.4}$-S and $LaWO_{0.6}N_{2.4}$-P; water redox potentials are also included, E_{fb}: flat band potential.

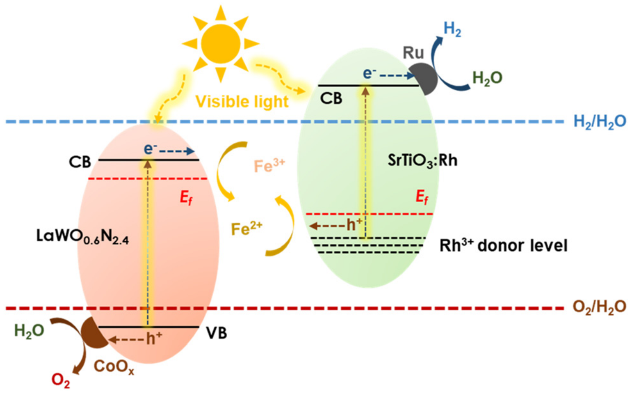

Fig. 6 Schematic illustration of the Z-scheme system employing Ru-loaded Rh-doped $SrTiO_3$ (Ru-$SrTiO_3$:Rh) as the H_2-evolution moiety and $LaWO_{0.6}N_{2.4}$-P thermally deposited with CoO_x as the O_2-evolution photocatalyst for visible light-driven overall water splitting. Conditions: 50 mg Ru-$SrTiO_3$:Rh and 50 mg CoO_x–$LaWO_{0.6}N_{2.4}$-P in 100 mL aqueous solution (2 mM $FeCl_3$, pH ~ 2.5 adjusted by HCl), light source 300 W Xe lamp coupled with a UV ($\lambda \geq 420$ nm) cutoff filter.

Schottky analysis (Fig. 5a and b) combined with XPS valence band scan data (Fig. 5c) suggests that the conduction and valence band edge of $LaWO_{0.6}N_{2.4}$ set approximately at 0.10 V and 1.3 V *vs.* RHE. A schematic illustration of band edge position is shown in Fig. 5d.

From the band edge alignment, one can quickly realize that $LaWO_{0.6}N_{2.4}$ cannot be a single-component photocatalyst for overall water splitting but can be an O_2-evolution photocatalyst for Z-scheme overall water splitting. As an exemplification, $LaWO_{0.6}N_{2.4}$-P was combined with Rh-doped $SrTiO_3$ ($SrTiO_3$:Rh), a typical H_2-evolution photocatalyst, to fabricate a Z-scheme system (Fig. 6). The so-formed system was capable of overall water splitting into stoichiometric H_2/O_2 evolution under visible light illumination ($\lambda \geq 420$ nm) in the presence of the Fe^{2+}/Fe^{3+} redox couple (Fig. 4d). Although XRD and FE-SEM analysis (Fig. S8 and S9†) suggest nearly no structural changes of $LaWO_{0.6}N_{2.4}$-P before and after photocatalytic experiment, N_2 evolution as well as XPS analysis (Fig. S10†) indicate that the following self-decomposition reactions occur.

$$2N^{3-} + 6h^+ \rightarrow N_2^{\uparrow} \tag{R1}$$

$$W^{4+} + h^+ \rightarrow W^{5+} \tag{R2}$$

$$W^{5+} + h^+ \rightarrow W^{6+} \tag{R3}$$

The self-decomposition reactions might be related to the poor oxidation power of photogenerated holes in $LaWO_{0.6}N_{2.4}$ whose valence band edge is close to the water oxidation potential. A more active cocatalyst would be useful to promote water oxidation reactions rather than oxidative self-decomposition reactions and will be our future work.

Conclusion

In summary, a narrow bandgap semiconductor, $LaWO_{0.6}N_{2.4}$, has been successfully synthesized in the form of porous single crystals ($LaWO_{0.6}N_{2.4}$ PSCs) from the topotactic conversion of $BiLaWO_6$. Photocatalytic tests suggest that it demonstrates superior activities for catalyzing water oxidation reactions under visible and infrared light illuminations. An AQE value as high as 0.13% at 800 ± 20 nm was recorded under optimal conditions, being the first near-infrared-light active oxynitride for photocatalytic water oxidation thus far. Moreover, its potential application was exemplified by constructing a Z-scheme system employing $LaWO_{0.6}N_{2.4}$ PSCs as the O_2-evolution moiety to achieve steady overall water splitting. This work not only provide us a porous single-crystaline $LaWO_{0.6}N_{2.4}$ with triggered photocatalytic performance for water oxidation reactions but also throws light on W-based perovskite oxynitrides with narrow bandgaps for solar energy conversions.

Author contributions

Mr Lin Yang performed the experiments. Dr Hui Duan analyzed the data. Prof. Xiaoxiang Xu administered the project and wrote the manuscript.

Conflicts of interest

There are no conflicts to declare.

Acknowledgements

We appreciate the financial support from the National Natural Science Foundation of China (Grant No. 51972233 and 52172225) and the Fundamental Research Funds for the Central Universities.

References

1 M. Thangamuthu, Q. S. Ruan, P. O. Ohemeng, B. Luo, D. W. Jing, R. Godin and J. W. Tang, Polymer photoelectrodes for solar fuel production: progress and challenges, *Chem. Rev.*, 2022, **122**, 11778–11829.

2 X. P. Tao, Y. Zhao, S. Y. Wang, C. Li and R. G. Li, Recent advances and perspectives for solar-driven water splitting using particulate photocatalysts, *Chem. Soc. Rev.*, 2022, **51**, 3561–3608.

3 T. Takata, J. Z. Jiang, Y. Sakata, M. Nakabayashi, N. Shibata, V. Nandal, K. Seki, T. Hisatomi and K. Domen, Photocatalytic water splitting with a quantum efficiency of almost unity, *Nature*, 2020, **581**, 411–414.

4 Y. B. Chen, X. Y. Feng, Y. Liu, X. J. Guan, C. Burda and L. J. Guo, Metal oxide-based tandem cells for self-biased

photoelectrochemical water splitting, *ACS Energy Lett.*, 2020, **5**, 844–866.

5 S. Ye, C. M. Ding, M. Y. Liu, A. Q. Wang, Q. G. Huang and C. Li, Water oxidation catalysts for artificial photosynthesis, *Adv. Mater.*, 2019, **31**, 1902069.

6 Z. Wang, Y. Inoue, T. Hisatomi, R. Ishikawa, Q. Wang, T. Takata, S. S. Chen, N. Shibata, Y. Ikuhara and K. Domen, Overall water splitting by Ta_3N_5 nanorod single crystals grown on the edges of $KTaO_3$ particles, *Nat. Catal.*, 2018, **1**, 756–763.

7 Q. Wang, M. Nakabayashi, T. Hisatomi, S. Sun, S. Akiyama, Z. Wang, Z. H. Pan, X. Xiao, T. Watanabe, T. Yamada, N. Shibata, T. Takata and K. Domen, Oxysulfide photocatalyst for visible-light-driven overall water splitting, *Nat. Mater.*, 2019, **18**, 827–832.

8 S. Lin, H. W. Huang, T. Y. Ma and Y. H. Zhang, Photocatalytic oxygen evolution from water splitting, *Adv. Sci.*, 2021, **8**, 2002458.

9 R. R. Pan, M. Hu, J. Liu, D. F. Li, X. D. Wan, H. Z. Wang, Y. M. Li, X. M. Zhang, X. L. Wang, J. Jiang and J. T. Zhang, Two-dimensional all-in-one sulfide monolayers driving photocatalytic overall water splitting, *Nano Lett.*, 2021, **21**, 6228–6236.

10 H. H. Li, J. D. Xiao, J. J. M. Vequizo, T. Hisatomi, M. Nakabayashi, Z. H. Pan, N. Shibata, A. Yamakata, T. Takata and K. Domen, One-step excitation overall water splitting over a modified Mg-doped $BaTaO_2N$ photocatalyst, *ACS Catal.*, 2022, **12**, 10179–10185.

11 K. H. Chen, J. D. Xiao, J. J. M. Vequizo, T. Hisatomi, Y. W. Ma, M. Nakabayashi, T. Takata, A. Yamakata, N. Shibata and K. Domen, Overall water splitting by a $SrTaO_2N$-based photocatalyst decorated with an Ir-promoted Ru-based cocatalyst, *J. Am. Chem. Soc.*, 2023, **145**, 3839–3843.

12 K. Maeda, D. L. Lu and K. Domen, Oxidation of Water under Visible-light irradiation over modified $BaTaO_2N$ photocatalysts promoted by tungsten species, *Angew. Chem., Int. Ed.*, 2013, **52**, 6488–6491.

13 T. Hisatomi, C. Katayama, Y. Moriya, T. Minegishi, M. Katayama, H. Nishiyama, T. Yamada and K. Domen, Photocatalytic oxygen evolution using $BaNbO_2N$ modified with cobalt oxide under photoexcitation up to 740 nm, *Energy Environ. Sci.*, 2013, **6**, 3595–3599.

14 J. Seo, D. Ishizuka, T. Hisatomi, T. Takata and K. Domen, Effect of Mg^{2+} substitution on the photocatalytic water splitting activity of $LaMg_xNb_{1-x}O_{1+3x}N_{2-3x}$, *J. Mater. Chem. A*, 2021, **9**, 8655–8662.

15 F. X. Zhang, A. Yamakata, K. Maeda, Y. Moriya, T. Takata, J. Kubota, K. Teshima, S. Oishi and K. Domen, Cobalt-modified porous single-crystalline $LaTiO_2N$ for highly efficient water oxidation under visible light, *J. Am. Chem. Soc.*, 2012, **134**, 8348–8351.

16 S. H. Wei, G. Zhang and X. X. Xu, Activating $BaTaO_2N$ by Ca modifications and cobalt oxide for visible light photocatalytic water oxidation reactions, *Appl. Catal., B*, 2018, **237**, 373–381.

17 Y. W. Wang, Y. Y. Kang, H. Z. Zhu, G. Liu, J. T. S. Irvine and X. X. Xu, Perovskite oxynitride solid solutions of $LaTaON_2$-$CaTaO_2N$ with greatly enhanced photogenerated charge separation for solar-driven overall water splitting, *Adv. Sci.*, 2021, **8**, 2003343.

18 Y. W. Wang, S. H. Wei and X. X. Xu, $SrTaO_2N$-$CaTaO_2N$ solid solutions as efficient visible light active photocatalysts for water oxidation and reduction, *Appl. Catal., B*, 2020, **263**, 118315.

19 K. Kawashima, M. Hojamberdiev, H. Wagata, E. Zahedi, K. Yubuta, K. Domen and K. Teshima, Two-step synthesis and visible-light-driven photocatalytic water oxidation activity of $AW(O,N)_3$ (A = Sr, La, Pr, Nd and Eu) perovskites, *J. Catal.*, 2016, **344**, 29–37.

20 W. J. Li, D. Li, X. Gao, A. Gurlo, S. Zander, P. Jones, A. Navrotsky, Z. J. Shen, R. Riedel and E. Ionescu, A study on the thermal conversion of scheelite-type ABO_4 into perovskite-type $AB(O,N)_3$, *Dalton Trans.*, 2015, **44**, 8238–8246.

21 K. Kawashima, Y. Liu, J. H. Kim, B. R. Wygant, I. Cheng, H. Celio, O. Mabayoje, J. Lin and C. B. Mullins, Infrared light-driven $LaW(O,N)_3$ OER photoelectrocatalysts from chloride flux-grown $La_4W_3O_{15}$ templating precursors, *ACS Appl. Energy Mater.*, 2019, **2**, 913–922.

22 J. D. Xiao, J. J. M. Vequizo, T. Hisatomi, J. Rabeah, M. Nakabayashi, Z. Wang, Q. Xiao, H. H. Li, Z. H. Pan, M. Krause, N. Yin, G. Smith, N. Shibata, A. Bruckner, A. Yamakata, T. Takata and K. Domen, Simultaneously tuning the defects and surface properties of Ta_3N_5 nanoparticles by Mg-Zr codoping for significantly accelerated photocatalytic H_2 evolution, *J. Am. Chem. Soc.*, 2021, **143**, 10059–10064.

23 Y. Q. Xiao, C. Feng, J. Fu, F. Z. Wang, C. L. Li, V. F. Kunzelmann, C. M. Jiang, M. Nakabayashi, N. Shibata, I. D. Sharp, K. Domen and Y. B. Li, Band structure engineering and defect control of Ta_3N_5 for efficient photoelectrochemical water oxidation, *Nat. Catal.*, 2020, **3**, 932–940.

24 J. Fu and S. E. Skrabalak, Enhanced Photoactivity from Single-crystalline $SrTaO_2N$ nanoplates synthesized by topotactic nitridation, *Angew. Chem., Int. Ed.*, 2017, **56**, 14169–14173.

25 S. S. Chen, T. Takata and K. Domen, Particulate photocatalysts for overall water splitting, *Nat. Rev. Mater.*, 2017, **2**, 17050.

26 M. Xiao, B. Luo, M. Q. Lyu, S. C. Wang and L. Z. Wang, Single-crystalline nanomesh tantalum nitride photocatalyst with improved hydrogen-evolving performance, *Adv. Energy Mater.*, 2018, **8**, 1701605.

27 C. A. Geiger, M. Grodzicki and G. Amthauer, The crystal chemistry and Fe-II-site properties of aluminosilicate garnet solid solutions as revealed by Mossbauer spectroscopy and electronic structure calculations, *Phys. Chem. Miner.*, 2003, **30**, 280–292.

28 C. Funke, T. Behm, R. Helbig, E. Schmid and S. Wurzner, Novel combination of orientation measurements and transmission microscopy for experimental determination of

grain boundary miller indices in silicon and other semiconductors, *J. Microsc.*, 2012, **246**, 70–76.

29 L. Jin, F. Y. Cheng, H. Li and K. Xie, Porous tantalum nitride single crystal at two-centimeter scale with enhanced photoelectrochemical performance, *Angew. Chem., Int. Ed.*, 2020, **59**, 8891–8895.

30 L. Yang, Q. Y. Fu, L. N. Wang, J. X. Yu and X. X. Xu, Liberating photocarriers in mesoporous single-crystalline $SrTaO_2N$ for efficient solar water splitting, *Appl. Catal., B*, 2022, **304**, 120934.

31 S. F. Chang, J. X. Yu, R. Wang, Q. Y. Fu and X. X. Xu, $LaTaON_2$ mesoporous single crystals for efficient photocatalytic water oxidation and Z-scheme overall water splitting, *ACS Nano*, 2021, **15**, 18153–18162.

32 L. Yang, J. X. Yu, Q. Y. Fu, L. L. Kong and X. X. Xu, Mesoporous single-crystalline $SrNbO_2N$: expediting charge transportation to advance solar water splitting, *Nano Energy*, 2022, **95**, 107059.

33 J. X. Yu and X. X. Xu, $LaNbON_2$ mesoporous single crystals with expedited photocarrier separation for efficient visible-light-driven water redox reactions, *J. Catal.*, 2022, **413**, 858–869.

34 C. W. Dong, S. Y. Lu, S. Y. Yao, R. Ge, Z. D. Wang, Z. Wang, P. F. An, Y. Liu, B. Yang and H. Zhang, Colloidal synthesis of ultrathin monoclinic $BiVO_4$ nanosheets for Z-scheme overall water splitting under visible light, *ACS Catal.*, 2018, **8**, 8649–8658.

35 B. H. Toby, EXPGUI, a graphical user interface for GSAS, *J. Appl. Crystallogr.*, 2001, **34**, 210–213.

36 R. Hesse, M. Weiss, R. Szargan, P. Streubel and R. Denecke, Improved peak-fit procedure for XPS measurements of inhomogeneous samples-Development of the advanced Tougaard background method, *J. Electron Spectrosc. Relat. Phenom.*, 2015, **205**, 29–51.

37 R. Abe, M. Higashi and K. Domen, Facile Fabrication of an efficient oxynitride TaON photoanode for overall water splitting into H_2 and O_2 under visible light irradiation, *J. Am. Chem. Soc.*, 2010, **132**, 11828–11829.

38 A. Watanabe, Polymorphism in Bi_2WO_6, *J. Solid State Chem.*, 1982, **41**, 160–165.

39 A. Watanabe, Synthesis and lattice-parameters of rare-earth bismuth tungstates, $BiLnWO_6$ and their solid-solutions, *Mater. Res. Bull.*, 1980, **15**, 1473–1477.

40 A. Kasahara, K. Nukumizu, T. Takata, J. N. Kondo, M. Hara, H. Kobayashi and K. Domen, $LaTiO_2N$ as a visible-light (≤600 nm)-driven photocatalyst (2), *J. Phys. Chem. B*, 2003, **107**, 791–797.

41 S. H. Wei and X. X. Xu, Boosting photocatalytic water oxidation reactions over strontium tantalum oxynitride by structural laminations, *Appl. Catal., B*, 2018, **228**, 10–18.